國立交通大學
National Chiao Tung University

UNIVERSITÀ DEGLI STUDI DI PADOVA

Laurea Magistrale in
ELECTRONIC ENGINEERING

Tesi di Laurea

Physics-Based Compact Model for p-GaN/AlGaN/GaN

Application: Understanding of Degradation after γ-Ray Irradiation

SUPERVISOR:
Matteo Meneghini

CO-SUPERVISOR:
Gaudenzio Meneghesso
Tian-Li Wu

AUTHOR:
Nicola Modolo

MATRICOLA:
1152960

ACADEMIC YEAR 2018/2019
8 JULY 2019

INNOSCIENCE EXHIBIT 1048
INNOSCIENCE v. EPC
IPR2023-01381

Physics-Based Compact Model for p-GaN/AlGaN/GaN HEMTs

Application: Understanding of Degradation After γ-Ray Irradiation

Abstract

Gallium Nitride (GaN)-based high electron mobility transistors (HEMTs) are rapidly emerging as front-runners in high-power mm-wave circuit applications. Despite the recent commercial success of GaN-based devices, internal physical mechanisms are often not completely understood. This thesis explores the nature of gallium nitride devices from the point of view of compact modeling paying particular attention to power electronic applications. To model the behaviour of such devices, the physics of the typical AlGaN/GaN Schottky HEMT is studied by solving the Schrödinger's and Poisson's equations in order to have a unified and accurate definition of the Fermi level and 2DEG charge.

The physical-based model is used to help our understanding of the effects of γ-irradiation on GaN-based devices. Thanks to this approach we demonstrate that we are able to point the leading factor in the induced degradation. Furthermore, we propose a novel approach to model the p-GaN/AlGaN/GaN structure by implementing the p-GaN layer in the developed AlGaN/GaN model. The simulation results are then compared with the experimental data obtained by four devices showing excellent agreement. Finally, inspired by the method used to include the p-GaN layer under the gate, and aware of the results that ferroelectric materials are showing in the rising NCFET technology, we studied the physics of such material following the phenomenological approach described by the Landau-Khalatnikov equations. The ferroelectric material is implemented in the AlGaN/GaN model. The simulations result is consistent with the studies conducted on the NCFET where the MFMIS structure shows higher ON-current, and transconductance.

Contents

Introduction **14**

1 Gallium Nitride **16**
1.1 HEMT working principle 16
1.2 GaN - Unique Material Properties 18
1.3 GaN - Impact 22

2 Modeling of D-Mode GaN HEMT **24**
2.1 GaN compact models: Overview 24
2.2 Core Model 26
2.2.1 Surface Potential 27
2.2.2 Intrinsic Charge 32
2.2.3 Drain Current 37
2.3 Real Device Effects 38
2.3.1 Mobility Degradation 39
2.3.2 Short Channel Effects 39
2.3.3 Access Region Resistance 40
2.4 Conclusion 42

3 Understanding of γ-Ray Degradation in Schottky HEMT **44**
3.1 Radiation Defects in GaN 44
3.1.1 Displacement Damage 44
3.2 γ-Ray Degradation in MIS-HEMT 48
3.2.1 Experiment Details 49
3.2.2 Experiment Results and Discussion 49
3.3 γ-Ray Degradation in Schottky HEMT 53
3.3.1 Device Fabrication and Experimental Results 53
3.3.2 Parameter Extraction Strategy 55
3.3.3 Understanding of γ-Ray Degradation using GaN Model 58
3.4 Conclusion 58

4 Modeling of E-Mode GaN HEMT **60**
4.1 Working Principle 60
4.2 Modeling the p-GaN HEMT 61
4.2.1 Voltage Drop in the p-GaN Layer 64
4.2.2 Fully Depleted p-GaN 68
4.3 Results 69
4.3.1 Gate Capacitance 70
4.3.2 Depletion Region 71

4.3.3 Vertical Potential Drop 75
4.3.4 I_D-V_G 76
4.4 Conclusion 77

5 Negative Capacitance in GaN HEMT **78**
5.1 Concept and Reasons 78
5.2 Ferroelectric Dynamics 80
5.2.1 Landau-Khalatnikov Model 81
5.2.2 Temperature Dependence 85
5.3 Device Implementation 88
5.3.1 Modeling NC-GaN HEMT 88
5.4 Conclusion 93

Conclusion and Future Work **94**

Chapter 4

Modeling of E-Mode GaN HEMT

4.1 Working Principle

As introduced in Chapter 1, GaN-based HEMTs are receiving significant attentions for high power, high frequency, and high efficiency power switching applications due to the advantage of GaN over the conventional silicon and to the possibility of manufacturing these devices at a comparable or lower cost than their aging Si-based competitors [55].

Despite the exceptional properties of GaN HEMTs, the inherent 2DEG not only provides a high mobility in the channel but also leads to an intrinsic normally-on characteristic. In practical power switching applications, enhancement-mode (E-mode) devices with positive threshold voltage (V_{TH}) are preferred compared to depletion-mode (D-mode) devices for consideration of fail-safe and simplifying the gate drive topology [56]. In the last years, different approaches, designed to fabricate normally-off HETMs, have been proposed [57], each one with different advantages/disadvantages:

(i) **Fluorine Implantation:** in the early stages, fluorine plasma ion implantation into the AlGaN or GaN gate region to deplete the channel showed good results. The main problem is that the stability of the threshold voltage strongly depends on the optimization of the implantation process [58].

(ii) **MIS/MOS-HEMTs with Recessed Gate:** in this case, the AlGaN layer is partially removed to contact the insulator with the GaN and reduce the electron concentration in the channel increasing the threshold voltage. However this method is sensitive to trapping-related degradation mechanisms, caused by defects at the GaN/insulator interface and/or in the bulk insulator, which under stress conditions can affect the shift of the threshold voltage [59].

(iii) **p-(Al)GaN/AlGaN/GaN:** characterized by a layer of (Al)GaN, doped with acceptor atoms such as magnesium (Mg), between the gate and the barrier layer, which causes the band diagram to rise from the gate side pulling the conduction band in the channel up and, consequently, opposing the formation of the 2DEG. However, p-types are characterized by long-term degradation and the difficulty related to its doping [56].

To date, the normally-off p-GaN solution seems to represent a promising technology because of the good trade-off between reliability and cost and is now available from

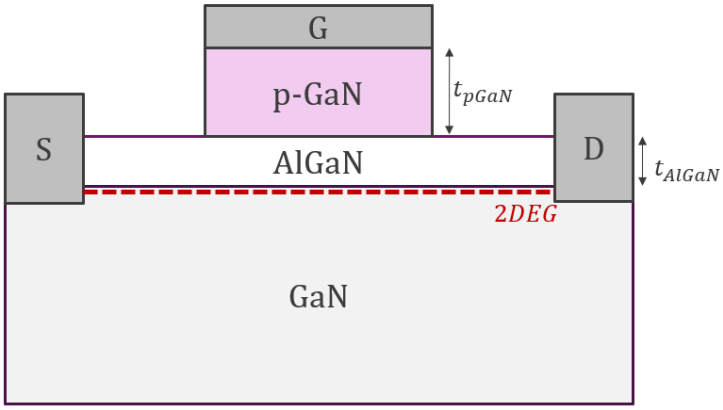

Figure 4.1: p-GaN/AlGaN/GaN HEMT structure discussed in this chapter where the p-GaN material is deposited under the gate of a Schottky HEMT device.

a broad range of suppliers [60]. In this type of structure, a Schottky contact is established between the top metal layer and the p-type semiconductor. However, relatively few data on the effect of the Schottky contact under the gate are available in literature [61].

To understand the phenomenological behavior of the gate vertical voltage drop in p-GaN HEMT, different models have been proposed [62, 63, 55, 56, 61]. These simplified analytical models always consider the gate as two back diodes. The top diode comes from the Schottky junction, while the bottom diode is similar to a PiN diode with the AlGaN acting as the "insulator" and the 2DEG as n-type semiconductor. The main limit of this approach is that the model of the equivalent circuit of the gate structure is made by only two back diodes, whose behavior is complicated to predict and varies depending on the bias, as reported by A. Stockman *et al.* [63] and N. Xu *et al.* [56]. This solution is not optimal and does not take into account the Schrödinger's and Poisson's equations that should be solved in order to have a precise understanding of what is happening in each layer under the gate.

Following the approach presented by T. L. Wu *et al.* [61], which investigates the p-GaN/AlGAN/GaN structure starting from its Capacitance-Voltage (C-V) characteristics, we propose a novel solution to understand the p-GaN HEMT using a physical-based model that defines the vertical voltage drop in the structure by solving the Schrödinger's and Poisson's equations. The developed model is implemented in the GaN model presented in Chapter 2 and is verified comparing the simulation results with the experimental data measured from four samples. The results give an unprecedented insight of the effect of the p-layer in the device; analyzing the gate capacitance, the thickness of the depletion region, the electric field and the vertical voltage drop in each layer under the gate.

4.2 Modeling the p-GaN HEMT

In order to understand the p-GaN/AlGaN/GaN structure (see figure 4.1), it is important to give a clear definition of the voltage drop in each layer of the structure. Figure 4.2 shows a detailed typical cross section of the device along with the energy-band diagram simulated using Synopsis' TCAD software where the Poisson's equa-

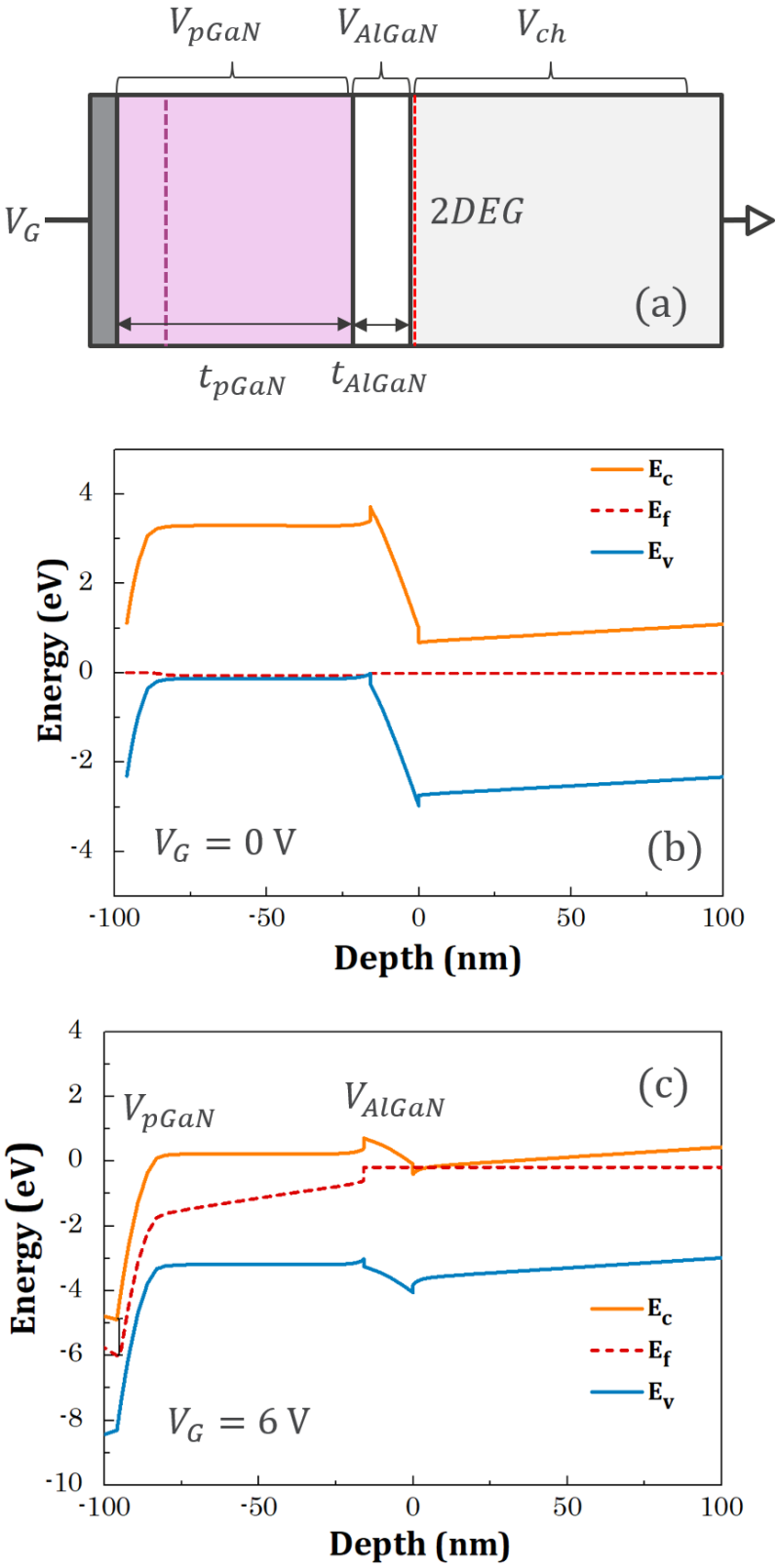

Figure 4.2: (a) Detailed cross section of the p-GaN/AlGaN/GaN structure with relative voltages along with the simulated energy-band diagram at (b) zero bias and (c) $V_G = 6$ V.

tion is solved self-consistently with the carrier continuity equations, taking into account the polarization charge [61]. From the energy band diagram we can see that the effect introduced by the p-GaN layer is to push down the Fermi level in the channel, causing the device to become normally-off. At zero bias (see figure 4.2b), the static voltage drop in each layer defines the threshold voltage of the device. The analysis of this important parameter has been exhaustively done by B. Bakeroot *et al.* [64] resulting in the following simplified equation:

$$V_{TH} = \psi_B + V_{bi} + \frac{\Delta E_{c1}}{q} - \frac{\Delta E_{c2}}{q} - V_b$$

where ψ_B is the Schottky barrier height of the metal towards the conduction band, V_{bi} the built-in potential of the Schottky contact, ΔE_{c1} the conduction band offset between the p-GaN and the AlGaN barrier, ΔE_{c2} the conduction band offset between the AlGaN and the GaN, and V_b the voltage barrier in the AlGaN resulting from the polarization and piezoelectric charge given by the unique polar properties of GaN materials. When a bias is applied, the vertical voltage drop is given by:

$$V_G = V_{TH} + V_{pGaN} + V_{AlGaN} + \psi_s(x) \tag{4.1}$$

where V_{pGaN} is the voltage drop in the p-GaN later and V_{AlGaN} is the voltage drop in the AlGaN which is dependent to the 2DEG charge:

$$V_{AlGaN} = \frac{q n_s}{\varepsilon_{AlGaN}} \cdot t_{AlGaN} \tag{4.2}$$

The surface potential $\psi_s(x)$ is strictly related with the energy of the electron in the 2DEG that is given by the Fermi level E_f and the channel potential dependence at any point x in the channel V(x):

$$\psi_s(x) = \frac{E_f}{q} + V(x)$$

It is interesting to see that equation 4.1 is the same as equation 2.3 introduced in Chapter 2 to model the AlGaN/GaN structure with the addition of the term V_{pGaN} to take into account the voltage drop in the p-GaN layer. This means that if V_{pGaN} is defined, the new structure can be implemented in the previously developed AlGaN/GaN model.

When a positive bias is applied (see figure 4.2), the surface potential $\psi_s(x)$ will start to increase until the energy of the electrons in the channel reaches the conduction band, leading to the formation of the 2DEG. Combining equations 4.1 and 4.2, the 2DEG charge can be expressed as follow:

$$n_s = \frac{\varepsilon_{AlGaN}}{q \cdot t_{AlGaN}} \cdot \left[V_G - V_{TH} - V_{pGaN} - \psi_s(x)\right] \tag{4.3}$$

The problem can be simplified if we assume a uniform charge distribution in the 2DEG, which is valid without loss of generality in case $V_S = V_D = 0$. In this case the surface potential is given by ψ_m and the charge in the channel is $q n_s = Q_{ch}$ leading to the following equation:

$$Q_{ch} = C_{AlGAN}\left[V_G - V_{TH} - V_{pGaN} - \psi_m\right] \tag{4.4}$$

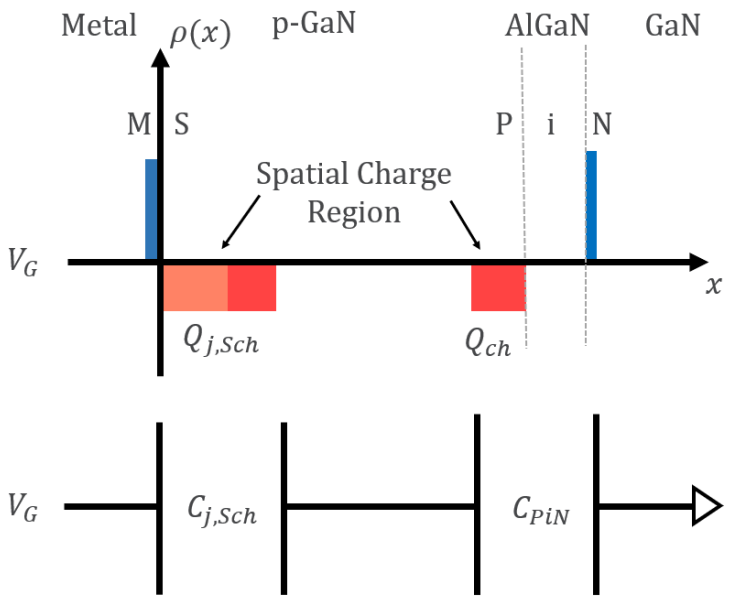

Figure 4.3: Qualitative representation of the charge distribution when a positive bias is applied in the p-GaN/AlGaN/GaN structure. Regarding the PiN junction the 2DEG channel can be considered equivalent to an highly doped n-type semiconductor.

4.2.1 Voltage Drop in the p-GaN Layer

V_{pGaN} is the result of two voltage drops: (i) is the drop in the metal/p-GaN contact which forms a Schottky junction and (ii) is the drop in the p-GaN/AlGaN contact which forms a PiN structure with the AlGaN as insulator and the two 2DEG as N-layer (see figure 4.3).

Schottky Junction

To model the Schottky junction we consider its depletion region like a series capacitance with C_{PiN} following the approach proposed by T. L. Wu *et al.* [61]. Consequently, they share the same dynamic charge:

$$dQ_{ch} = C_{PiN}\, dV_{PiN} = C_{j,Sch}\, dV_{j,Sch}$$

The Schottky junction capacitance is given by:

$$\boxed{C_{j,Sch} = \frac{C_{j0}}{\left(1 + \dfrac{V_{j,Sch}}{V_{bi}}\right)^{m}}} \tag{4.5}$$

where $m = (0 \sim 1)$ is a dimensionless non-ideality factor usually used to describe the non-uniformity of the doping profile [65]. In case of non-uniform doping:

$$Q = q \int_0^{x_d} N(x)\, dx \tag{4.6}$$

Then:

$$C = \frac{dQ}{dV} = \frac{dQ}{dx} \cdot \frac{dx}{dV}$$
$$= qN(x)\frac{dx}{dV}$$
$$= qN(x)\frac{dx}{dC} \cdot \frac{dC}{dV}$$

where:

$$\frac{dx}{dC} = \varepsilon \frac{d(C^{-1})}{dC} = -\frac{\varepsilon}{C^2} \Longrightarrow \quad qN(x) = -\frac{C^3}{q\varepsilon \cdot \dfrac{dC}{dV}} \tag{4.7}$$

From equation 4.5, equation 4.7 can be divided in:

$$\left.\begin{array}{ll} \text{(i)} & \dfrac{dC}{dV} = -\dfrac{mC_{j0}}{V_{bi}}\left(1+\dfrac{V}{V_{bi}}\right)^{-1-m} \\ \text{(ii)} & C^3 = C_{j0}^3\left(1+\dfrac{V}{V_{bi}}\right)^{-3m} \end{array}\right\} \quad \frac{\text{(ii)}}{\text{(i)}} = -\frac{V_{bi}C_{j0}^2}{m}\left(1+\frac{V}{V_{bi}}\right)^{1-2m}$$

Finally, the non-uniform doping profile can be expressed as:

$$N(V) = \frac{V_{bi}C_{j0}^2}{q\varepsilon m}\left(1+\frac{V}{V_{bi}}\right)^{1-2m}$$

$$\text{If} \quad C_{j0} = \sqrt{\frac{qN_A\varepsilon}{2V_{bi}}} \quad \Longrightarrow \quad N(V) = \frac{N_A}{2m}\left(1+\frac{V}{V_{bi}}\right)^{1-2m} \tag{4.8}$$

From equation 4.8 we can see that if (1) $m < 1/2$, $N(V)$ will increase with the increase of the voltage and if (2) $m > 1/2$, N(V) will decrease. To verify the result just obtained in equation 4.8, we can start from the equation that relates the thickness of the depletion region and the capacitance of equation 4.5:

$$x_d = \frac{\varepsilon}{C} = \sqrt{\frac{2\varepsilon V_{bi}}{qN_A}}\left(1+\frac{V}{V_{bi}}\right)^{m} \tag{4.9}$$

Then:

$$\frac{dx}{dV} = \frac{m}{V_{bi}}\sqrt{\frac{2\varepsilon V_{bi}}{qN_A}}\left(1+\frac{V}{V_{bi}}\right)^{m-1}$$

$$\Longrightarrow \quad dx = \frac{m}{V_{bi}}\sqrt{\frac{2\varepsilon V_{bi}}{qN_A}}\left(1+\frac{V}{V_{bi}}\right)^{m-1} dV$$

From equation 4.6, combined with equations 4.8 and 4.9:

$$Q = q\int_0^{x_d} N(x)\,dx = q\int_0^{V} N(V)\cdot\frac{m}{V_{bi}}\sqrt{\frac{2\varepsilon V_{bi}}{qN_A}}\left(1+\frac{V}{V_{bi}}\right)^{m-1}dV$$

$$= \int_0^{V}\frac{qN_A}{2m}\left(1+\frac{V}{V_{bi}}\right)^{1-2m}\frac{m}{V_{bi}}\sqrt{\frac{2\varepsilon V_{bi}}{qN_A}}\left(1+\frac{V}{V_{bi}}\right)^{m-1}dV \tag{4.10}$$

$$= \int_0^{V}\sqrt{\frac{qN_A\varepsilon}{2V_{bi}}}\left(1+\frac{V}{V_{bi}}\right)^{-m}dV = \int_0^{V} C\,dV$$

Analyzing equations 4.5, 4.8, 4.9, and 4.10, we can see that charge, capacitance, non-uniform doping and thickness are all correctly related, meaning that the model is self-consistent. From equation 4.10, the charge depleted in the Schottky junction can be calculated solving the integral:

$$\boxed{Q_{j,Sch} = \frac{V_{bi}}{1-m}\sqrt{\frac{qN_A\varepsilon_{GaN}}{2V_{bi}}}\left(1+\frac{V_{j,Sch}}{V_{bi}}\right)^{1-m}} \tag{4.11}$$

Since, the Schottky capacitance can be considered in series with the PiN capacitance, the charge $C_{j,Sch}$ is the sum of the static charge Q_0 that corresponds to equation 4.11 at zero bias, and the dynamic charge Q_{ch} (see figure 4.3):

$$\begin{cases} Q_{j,Sch} = Q_0 + Q_{ch} \\ Q_0 = \dfrac{V_{bi}}{1-m}\sqrt{\dfrac{qN_A\varepsilon_{GaN}}{2V_{bi}}} \end{cases} \tag{4.12}$$

Combining equation 4.11 and equation 4.12 and squaring both sides we obtain:

$$(Q_0+Q_{ch})^2 = \left(Q_{j,Sch}\right)^2$$

$$(Q_0+Q_{ch})^2 = \left[Q_0\cdot\left(1+\frac{V_{j,Sch}}{V_{bi}}\right)^{1-m}\right]^2(Q_0+Q_{ch})^2$$

$$\Longrightarrow \quad V_{j,Sch} = V_{bi}\cdot\left[\left(1+\frac{Q_{ch}}{Q_0}\right)^{\frac{1}{1-m}}-1\right]$$

The voltage drop in the Schottky junction can be expressed as:

$$\boxed{V_{j,Sch} = V_{bi}\cdot\left[\left(1+Q_{ch}\cdot\sqrt{\frac{2(1-m)^2}{qN_A\varepsilon_{GaN}V_{bi}}}\right)^{\frac{1}{1-m}}-1\right]} \tag{4.13}$$

In case of uniform doping where $m = 1/2$, equation 4.13 becomes:

$$\boxed{V_{j,Sch} = \frac{Q_{ch}^2 + 2Q_{ch}\sqrt{2qN_A\varepsilon_{GaN}V_{bi}}}{2qN_A\varepsilon_{GaN}}} \tag{4.14}$$

From equation 4.14, it is interesting to observe that:

(i) at zero bias the device is off, $Q_{ch} = 0$, and the dynamic voltage drop in the Schottky junction is zero;

(ii) the voltage drop in the p-GaN is inversely proportional to the doping level;

(iii) $V_{j,Sch}$ has a quadratic dependence with the gate charge while the AlGaN layer $V_{AlGAN} = Q_{ch}/C_{AlGaN}$ is linearly dependent.

PiN Junction

To model the voltage drop in the PiN junction, it is important to assume that the 2DEG channel is equivalent to a particular highly doped n-type semiconductor where the doping level is modulated by the charge density in the channel and therefore by the gate voltage. The analysis starts from equation 4.15, which describes the relationship between the electric field of the p-type semiconductor and the insulator contacts under the simplified assumption that there is no surface charge present between the p-GaN and the AlGaN:

$$\varepsilon_{GaN}\mathscr{E}_P = \varepsilon_{AlGaN}\mathscr{E}_{AlGaN} \tag{4.15}$$

The two electric fields are defined as:

$$\begin{cases} \mathscr{E}_P = \dfrac{qN_A}{\varepsilon_{GaN}}t_P \\ \mathscr{E}_{AlGaN} = \dfrac{qn_s}{\varepsilon_{AlGaN}} \end{cases} \tag{4.16}$$

Combining equations 4.15 and 4.16 leads to:

$$\begin{aligned} qN_A t_P &= qn_s \\ \implies \quad t_P &= \frac{n_s}{N_A} \end{aligned} \tag{4.17}$$

Equation 4.17 express the thickness of the depletion region in the p-GaN/AlGaN contact as proportional with the charge in the channel and inversely proportional with the Mg concentration in the p-GaN. From equation 4.6 and under the assumption of uniform distribution, which is valid without loss of generality in case $V_S = V_D = 0$, we can relate the gate charge with t_P:

$$\boxed{t_P = \frac{Q_{ch}}{qN_A}} \tag{4.18}$$

The potential drop in the p-GaN is given by:

$$V_P = \int_0^{t_P} \mathscr{E}_P \, dx = \frac{qN_A}{2\varepsilon_{GaN}} t_P^2 \tag{4.19}$$

Combining equations 4.18 and 4.19:

$$\boxed{V_P = \frac{Q_{ch}^2}{2qN_A\varepsilon_{GaN}}} \tag{4.20}$$

From equation 4.20, which describes the dynamic voltage drop in the p-GaN/AlGaN contact, we can do the same considerations of equation 4.14, observing that:

(i) at zero bias the device is off, $Q_{ch} = 0$, and the dynamic voltage drop in the p-GaN/AlGaN contact is zero;

(ii) the voltage drop in the p-GaN is inversely proportional to the doping level;

(iii) V_P has a quadratic dependence with the gate charge. This means that for high voltages, the voltage drop in the p-layer will become predominant.

The total drop in the p-GaN layer is given by the contribution of both equations 4.13 and 4.20, which in case of uniform doping with $m = 1/2$ becomes:

$$\boxed{V_{pGaN} = \frac{Q_{ch}^2 + Q_{ch}\sqrt{2qN_A\varepsilon_{GaN}V_{bi}}}{qN_A\varepsilon_{GaN}}} \tag{4.21}$$

4.2.2 Fully Depleted p-GaN

The thickness of the p-GaN is an important parameter to take into account. From equation 4.21, we see that the extension of the depletion region is inversely proportional to the doping level in the p-GaN. If the Mg concentration is low enough, the depletion region will extend significantly up to the case of a fully depleted device. In case of fully depleted p-GaN layer, the Space Charge Region (SCR) cannot continue to increase and the relative capacitance becomes constant and equal to:

$$C_{fd} = \frac{\varepsilon_{GaN}}{t_{pMAX}}$$

To have a smooth and continuous transition, we propose to solve the problem starting from the definition of voltage drop in a fully depleted device. In this case the capacitance is constant and the voltage drop is given by:

$$\boxed{V_{fd} = \frac{Q_{ch}}{C_{fd}} = Q_{ch} \cdot \frac{t_{pMaX}}{\varepsilon_{GaN}}} \tag{4.22}$$

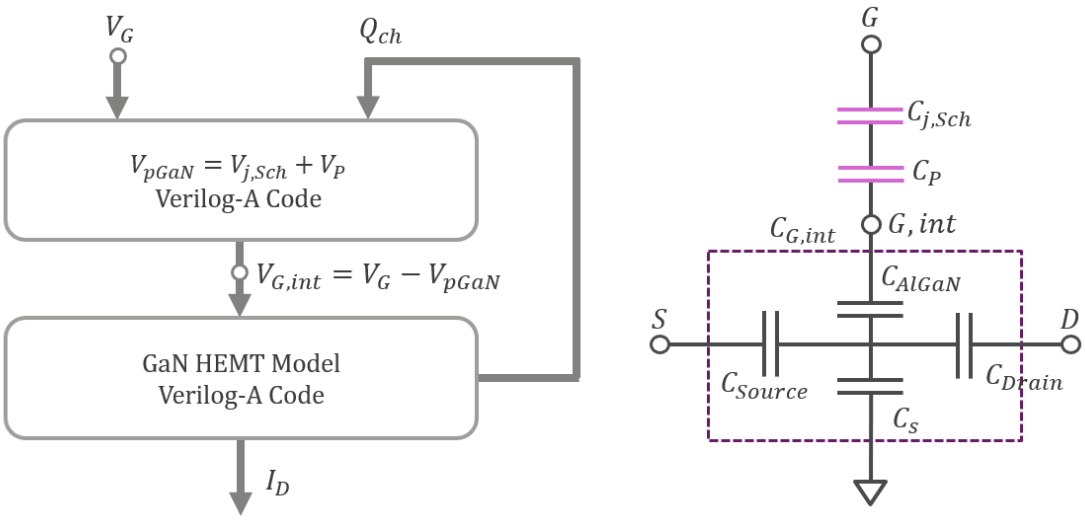

Figure 4.4: Modeling flow-chart used to simulate the p-GaN/AlGaN/GaN structure next to its equivalent circuit

Equations 4.21 and 4.22 can be interpolated using the following classic interpolation scheme:

$$V_{p,eff} = \frac{V_{pGaN}}{\sqrt[k]{1+\left(\frac{V_{pGaN}}{V_{fd}}\right)^k}} \tag{4.23}$$

where k is an interpolation coefficient with default value $k = 2$. Using this expression to define the voltage drop in the p-GaN layer, we take into account the fact that the SCR cannot extent above a maximum value t_{pMAX}.

The calculation of the charge in the channel which is strongly related with the surface potential and therefore the Fermi level (see equation 4.4), can be obtained solving the Schrödinger's and Poisson's equations. This is done by different physics-based compact models [31, 29, 30], each one with a different algorithm.

In this case, the p-layer has been implemented using Verilog-A in the core model presented in Chapter 2. Figure 4.4 shows the modeling flow-chart used to simulate the p-GaN/AlGaN/GaN structure next to its equivalent circuit. The new developed model has been used to study the impact of the p-type layer starting from the device measurements of four samples.

4.3 Results

To verify the developed mode, it has been used to fit the experimental data of four samples. The heterostructures are grown by MOCVD on a 200 mm silicon (111) substrate. A 70 nm Mg-doped p-type GaN is grown on top of an epitaxial stack consisting of an AlN nucleation layer, GaN buffer layer, GaN channel, and 16 or 12.5 nm $Al_{0.25}Ga_{0.75}N$ barrier layer.

Two different flows in growing the last p-type GaN ayer are used [61]. To investigate the C-V characteristics, a simple 75 μm × 75 μm is fabricated. A summary of the important process parameters can be found in table 4.1.

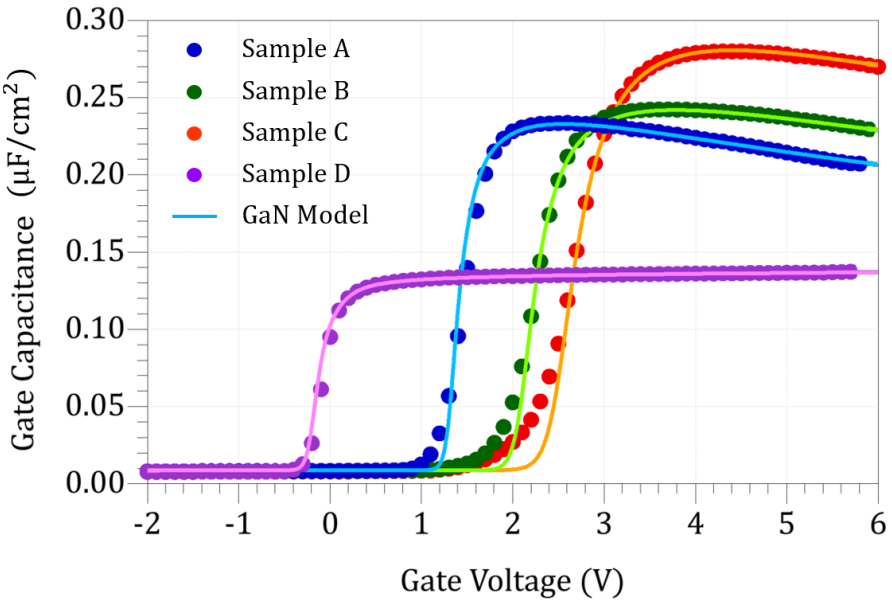

Figure 4.5: Measured and simulated C-V characteristic. The simulation shows excellent agreement with the experimental data for all the samples. In case of Samples A, B, and C, with the increase of the gate voltage it follows the decrease of the capacitance due to the increase of the depletion region thickness, while in case of Sample D which has a fully depleted p-GaN it remains constant.

4.3.1 Gate Capacitance

In figure 4.5 the simulation and the measured experimental data are compared showing excellent agreement and demonstrating that the new developed model is able to include the effect of the p-GaN layer. Since the developed model is physical based, it allows an unprecedented insight of the effect of each layer in the structure. In fact, the total gate capacitance is the resulting of the series of the Schottky junction, the PiN junction and the surface capacitance:

$$C_G = \left(\frac{1}{C_{j,Sch}} + \frac{1}{C_{PiN}} + \frac{1}{C_s} \right)^{-1} \tag{4.24}$$

In figure 4.6, the contribution given by each series capacitor is plotted for Sample A. The three capacitance are sharing the same dynamic charge dQ_{ch}, so their relative

	Sample A	Sample B	Sample C	Sample D
Mg flow	Low	Medium	Medium	Very Low
AlGaN	16 nm	16 nm	12.5 nm	16 nm
$L \times W$	75 × 75 μm	75 × 75 μm	75 × 75 μm	75 × 75 μm
Al	25%	25%	25%	25%
p-GaN	70 nm	70 nm	70 nm	70 nm

Table 4.1: Summary of the important device parameters of Samples A,B,C, and D.

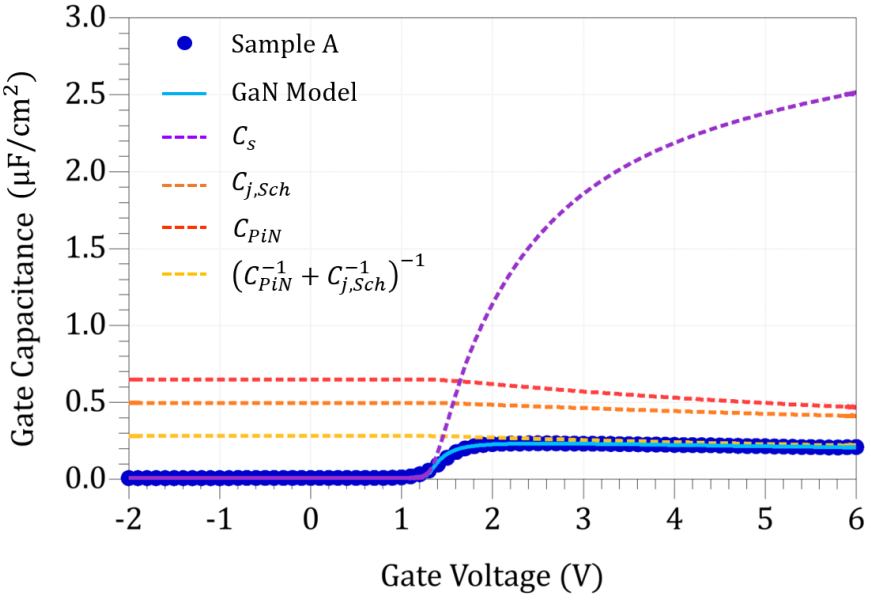

Figure 4.6: Contribution of each capacitance in the p-GaN/AlGaN/GaN structure for the calculation of the total capacitance C_G of Sample A. For $V_G > V_{TH}$, when the 2DEG is formed, the surface capacitance C_s becomes big enough to be considered negligible in the calculation of the total capacitance C_G.

values can be calculated from the respective voltage drop as:

$$C_x = \frac{dQ_{ch}}{dV_x}$$

In figure 4.7(a, b, c, and d), the effect of the Schottky junction capacitance in series with the PiN capacitance is highlighted for Samples A, B, C, and D respectively. Unlike MIS-HEMT, where the total capacitance is the series capacitance of the two insulator layers in the stack, the p-GaN introduces the effect of lowering the total gate capacitance as the gate voltage increases, as a consequence of the increase of the SCR thickness. Since the developed model is physical-based, the number of parameters is reduced and the extraction is facilitate.

Table 4.2 shows the extracted parameters for Samples A, B, C and D. The extracted N_A indicates that in Samples A, B, and C the Mg concentration is always around 10^{19} cm^{-3}. The main reason why Sample C looks higher compared to Sample A and B is due to the thickness of the AlGaN, which is 12.5 nm in Sample C and 16 nm in Sample A and B.

4.3.2 Depletion Region

In Sample D, the gate capacitance behaves differently because the Mg concentration is significantly lower compared to the other three samples. In this case C_G is constant and the p-layer can be considered fully depleted since the SCR is not extending anymore. From figure 4.7d, we can see that at a sufficiently high gate voltage, for example $V_G = 4$ V, the contribution of C_s can be neglected and the gate capacitance is given simply by C_{PiN} and $C_{j,Sch}$. In the fully depleted case this is

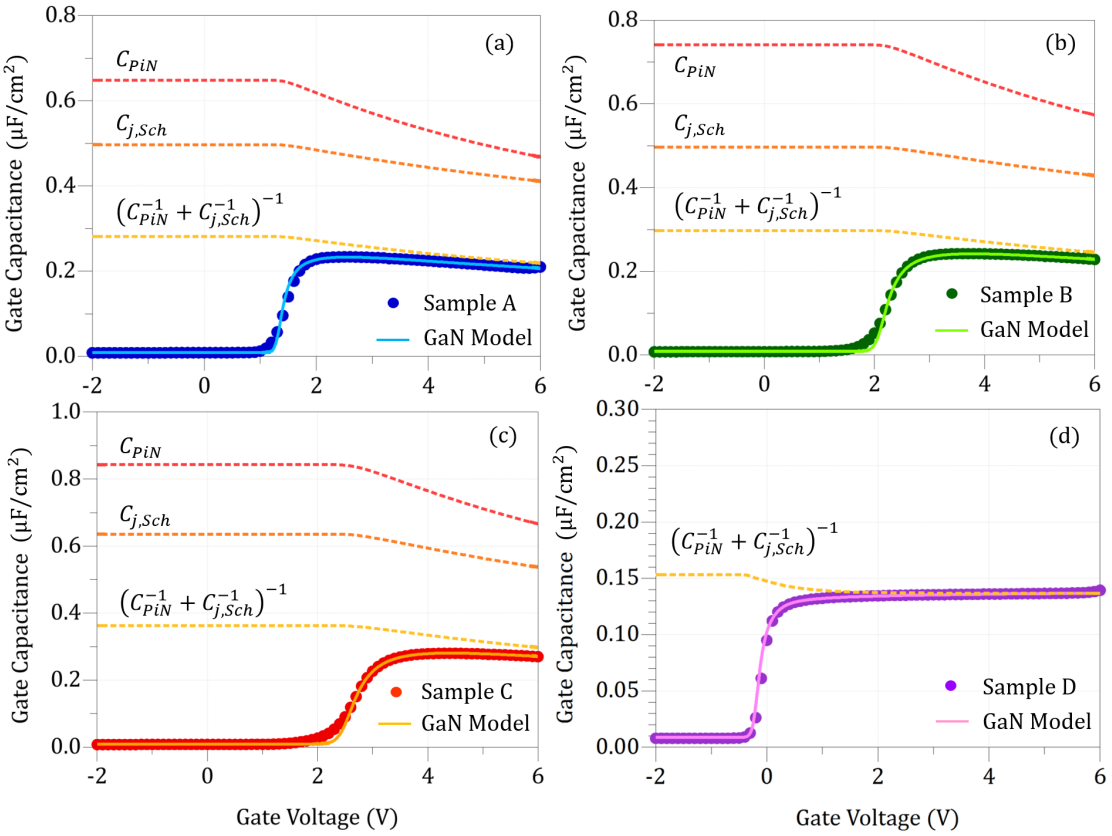

Figure 4.7: Detail of the effect of the Schottky and the PiN junction lowering the total capacitance when the gate voltage increases for Samples A, B, and C. In case of Sample D the device is fully depleted so since the voltage drop is defined by the interpolation of equations 4.21 and 4.22, it becomes hard to distinguish the single effect of the Schottky junction and the PiN junction. For this reason only their total contribution is plotted.

equivalent to:

$$C_G = \left(\frac{t_{pMAX}}{\varepsilon_{GaN}} + \frac{t_{AlGaN}}{\varepsilon_{AlGaN}} \right)^{-1}$$

The maximum extension of the depletion region can be extracted:

$$t_{pMAX} = \varepsilon_{GaN} \cdot \left(\frac{1}{C_G} - \frac{t_{AlGaN}}{\varepsilon_{AlGaN}} \right)$$

As we can see in table 4.2, the extracted value is $t_{pMAX} = 41.5$ nm which is smaller than the expected $t_{pGaN} = 70$ nm. This means that the depletion region in a fully depleted device is not extending along all the p-GaN layer but it will saturate at a maximum value $t_{pMAX} < t_{pGaN}$.

To have an intuition of the reason why this happens, in figure 4.10 a qualitative representation of the charge distribution in the two series capacitors is plotted. When the gate voltage increases, the thickness of the depletion region in both contacts increases causing the decrease of the corresponding capacitance.

Under the assumption that the charge in the plates of the capacitance must be the same, the extension of the depletion region will continue to increase until the charge N_A in the p-type semiconductors is enough to guarantee that the charge in

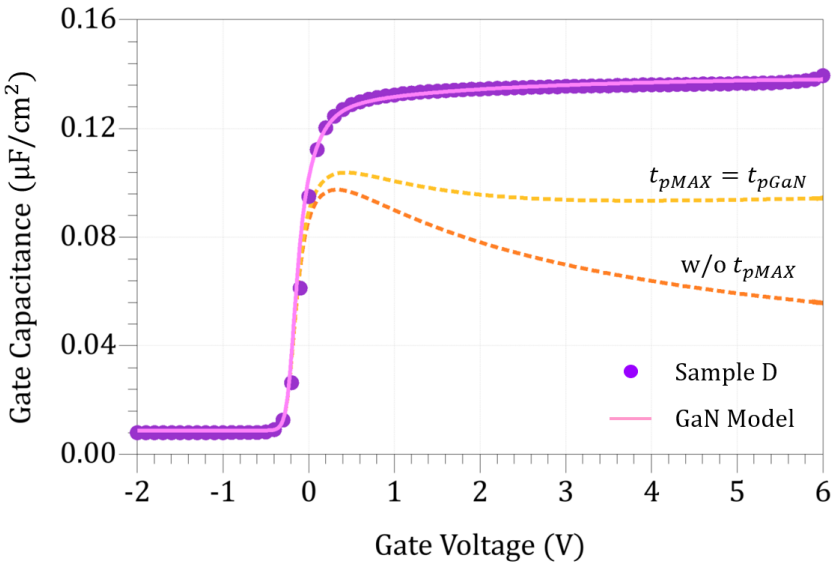

Figure 4.8: Simulation result of Sample D setting the maximum extension of the depletion region equal to the thickness of the p-GaN layer and without taking into account the maximum extension of the depletion region.

the two plates of the PiN capacitance is balanced. If the entire p-layer is emptied the 2DEG should disappear to maintain the conservation of the charge. For this reason $t_{pMAX} < t_{pGAN}$.

Figure 4.8 shows the result of the simulation conducted on Sample D comparing the cases $t_{pMAX} = 41.5$ nm with $t_{pMAX} = t_{pGAN} = 70$ nm, and $t_{pMAX} = \infty$. If $t_{pMAX} = t_{pGAN} = 70$ nm, at $V_G = 4$ V the gate capacitance becomes too small, confirming that the depletion region is not extending along all the p-GaN layer. If the maximum extension of the SCR is not considered and equation 4.21 is used instead of equation 4.23, the gate capacitance will continue to decrease.

The extracted $t_{pMAX} = 42$ nm is significantly smaller compared to the p-GaN thickness because in case of Sample D the doping level is very low. Since for Samples A, B, and C the doping is very high and consequently the effect introduced by

	Unit	Sample A	Sample B	Sample C	Sample D
N_A	cm^{-3}	1.35×10^{19}	1.75×10^{19}	2.2×10^{19}	4×10^{17}
V_{bi}	V	1.95	1.95	1.95	1.2
V_{TH}	V	1.5	2.4	2.9	0.1
C_{GSO}	$\mu F/cm^2$	0.008	0.008	0.008	0.008
t_{pMAX}	nm	65	65	65	42
n_{factor}	-	0.5	1.5	2.5	0.5
m	-	0.5	0.5	0.5	0.5
k	-	3	3	3	3

Table 4.2: Summary of the extracted parameters for Samples A,B,C, and D.

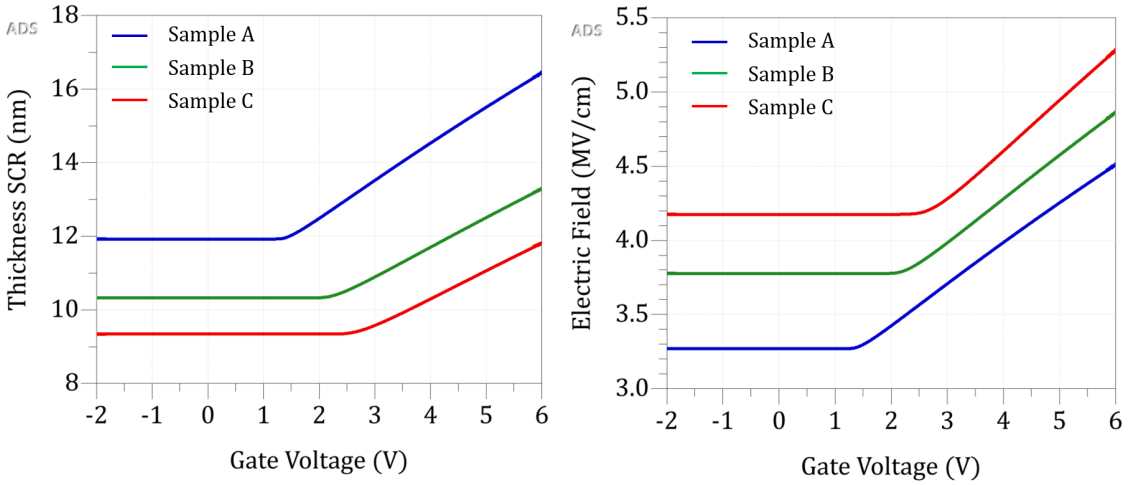

Figure 4.9: Depletion region in Sample A, B, and C next to the corresponding Electric field in the Schottky junction.

the saturation of the depletion region is almost negligible. With this assumption, the thickness and the electric field in the Schottky junction can be calculated as:

$$\begin{cases} t_{j,Sch} = \dfrac{\varepsilon_{GaN}}{C_{j,Sch}} = \sqrt{\dfrac{2\varepsilon_{GaN}V_{bi}}{qN_A}}\left(1+\dfrac{V_{j,Sch}}{V_{bi}}\right)^m \\ \mathscr{E}_{j,Sch} = \dfrac{2(V_{bi}+V_{j,Sch})}{t_{j,Sch}} \end{cases} \tag{4.25}$$

Figure 4.9 shows that in case of high Mg concentration, the average thickness of the Schottky junction is around $t_{j,Sch} = 13$ nm with an electric field of $\mathscr{E}_{j,Sch} = 3.7$ MV/cm. In Chapter 1 table 1.1 we can see that the breakdown voltage in GaN materials is around 3.3 MV/cm which is slightly smaller than the average simulated electric field in the Schottky junction. The value of $\mathscr{E}_{j,Sch}$ is particularly high also

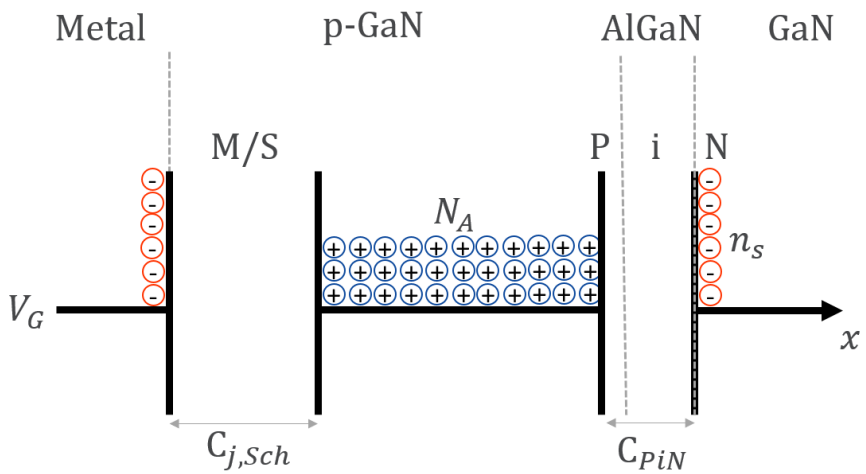

Figure 4.10: Qualitative representation of the charge distribution in the two series capacitance. To keep the charge balanced, the p-layer cannot be completely depleted.

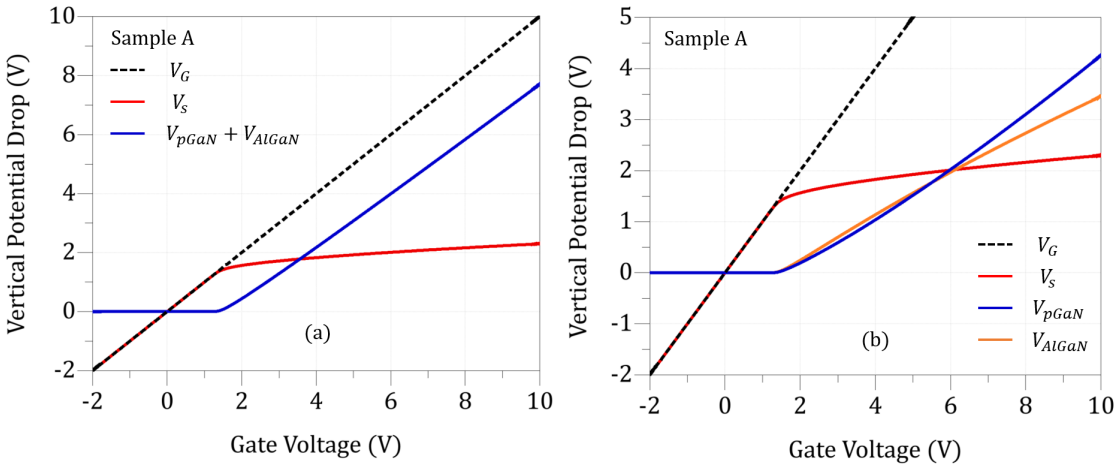

Figure 4.11: Vertical voltage drop in the channel vs voltage drop in the p-GaN and AlGaN layers. The simulation is calibrated with the extracted parameters of Sample A.

at zero bias confirming that such magnitude is not dependent from the model but from the material parameters. In fact at zero bias the electric field is:

$$\mathscr{E}_{j0} = \frac{2V_{bi}}{t_{j0}} = \sqrt{\frac{2qN_A V_{bi}}{\varepsilon_{GaN}}} \tag{4.26}$$

where t_{j0} is the thickness of the deletion region at zero bias. Here, it is important to observe that this is not the average electric field in the Schottky junction but the maximum electric field at the metal-semiconductor interface. The average electric field along the depletion region can be calculated as:

$$\mathscr{E}_{j,m} = \frac{\mathscr{E}_{j,MAX} + \mathscr{E}_{j,MIN}}{2} = \frac{\mathscr{E}_{j,MAX}}{2} \sim 1.8\,MV/cm \tag{4.27}$$

which is smaller than $\mathscr{E}_{BR} = 3.3$ MV/cm. Furthermore, it has to considered that the model of the metal/semiconductor interface ignored some possible effects that take place when the metal is deposited on the GaN material such as inhomogenities, dangling bond and any abrupt change at the interface.

4.3.3 Vertical Potential Drop

Thanks to the developed model, we can give an unprecedented insight of the potential drop in each layer of the device. To do so, we will not consider the voltage drop at zero bias given by the static elements of the heterojunction such as work function, built-in potential, piezoelectric polarization charge, and conduction band offset [64], but only the dynamic potential, to see how it is divided in each layer of the device with the increase of the gate voltage.

Figure 4.11 shows the vertical voltage drop in the p-GaN/AlGaN/GaN structure while fitting the experimental data of Sample A. In figure 4.11a it is possible to see that:

- if $V_G < V_{TH}$ the increase of the gate voltage is all taken by the channel which sees an increase of the Fermi level until it reaches the conduction band and the 2DEG is formed;

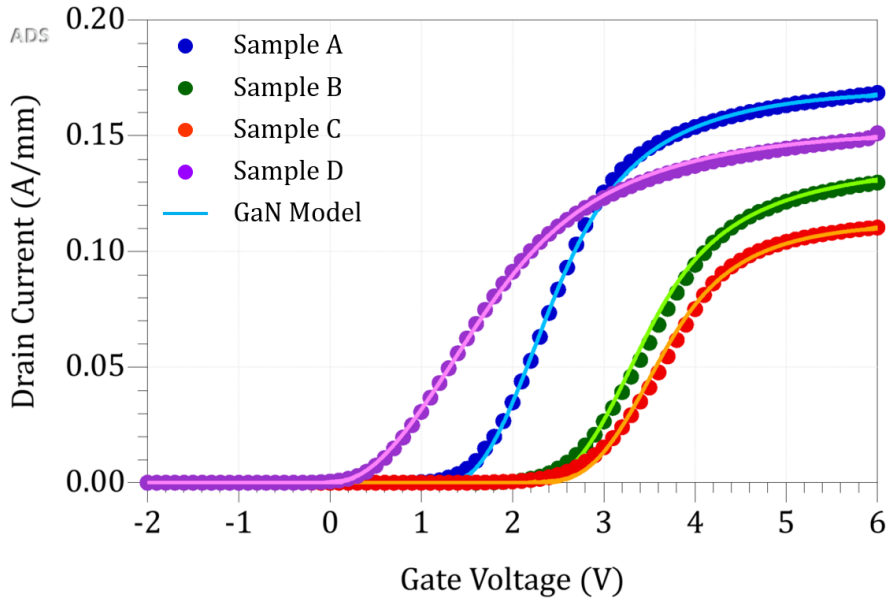

Figure 4.12: Measured and simulated I_D-V_G characteristic. The simulation shows good agreement with the experimental data for all the samples.

- if $V_G > V_{TH}$, the potential in the channel is almost saturated and the increase in the gate voltage is taken by the p-GaN and he AlGaN layer.

In figure 4.11b we can see in detail how the voltage drop is divided between the p-GaN and AlGaN. In case of high doping, the two drops are almost the same for all the operation region since V_{pGaN} is inversely proportional to the doping level as we can see in equation 4.23. If the simulation is conducted up to 10 V, at a certain moment, the p-GaN voltage will become dominant since its dependence with Q_{ch} is quadratic while for the AlGaN is linear. The same considerations are valid also for Sample B and C.

4.3.4 I_D-V_G

To conclude the developed physical-based model of the p-GaN/AlGaN/GaN HEMT has been used to fit the I_D-V_G measurements for each sample showing a good agree-

	Unit	Sample A	Sample B	Sample C	Sample D
$L \times W$	μm	0.8×100	0.8×100	0.8×100	0.8×100
μ_0	cm^2/Vs	1400	1100	1000	1400
μ_a	-	5×10^{-9}	7×10^{-9}	9×10^{-9}	2×10^{-9}
μ_b	-	5×10^{-17}	3×10^{-17}	6×10^{-17}	8×10^{-17}
v_S	cm/s	1.1×10^5	1.1×10^5	1.1×10^5	1.1×10^5
$n_{s,acc}$	cm^{-2}	7.5×10^{12}	7.5×10^{12}	7.5×10^{12}	6.5×10^{12}

Table 4.3: Summary of the extracted parameters for Samples A,B,C, and D.

ment with the experimental data and confirming the validity of the model. Figure 4.12 shows the result of the simulation compared with the measured drain current while tables 4.2 and 4.3 indicate all the extracted parameters. The meaning of all these parameters is explained in Chapter 2. The velocity saturation and the mobility in the access region are assumed to be the same as in the channel.

4.4 Conclusion

In this chapter, we proposed a novel approach to extend the GaN model developed in Chapter 2, including a p-GaN layer under the gate of the AlGaN/GaN structure. To the best of the knowledge of the author this is the first time a physical-based compact model includes such structure. The physics and the strategy used to implement the Verilog-A code has been well explained and verified comparing the simulation results with the experimental data measured on four different devices. Inspired by the method used in this chapter to include the p-GaN layer under the gate, and aware of the results that ferroelectric materials are showing, in the rising NCFET technology, when deposited under the gate of Si-based devices, the main objective of the next chapter study is to try to implement the negative capacitance in the AlGaN/GaN model to study how this unique material can improve the DC performance of GaN-based devices.

Bibliography

[1] Y.S. Chauhan et al. *FinFET Modeling for IC Simulation and Design: Using the BSIM-CMG Standard*. Elsevier Science, 2015. ISBN: 9780124200852. URL: https://books.google.com.tw/books?id=nXGDBAAAQBAJ.

[2] U. Mishra and J. Singh. *Semiconductor Device Physics and Design*. Series on Integrated Circuits and Systems. Springer Netherlands, 2007. ISBN: 9781402064807. URL: https://books.google.com.tw/books?id=6NAtk7zr3n4C.

[3] J. Piprek. *Nitride Semiconductor Devices: Principles and Simulation*. Wiley, 2007. ISBN: 9783527610716. URL: https://books.google.com.tw/books?id=iDiGR5Un5xoC.

[4] R.S. Muller and T.I. Kamins. *Device Electronics for Integrated Circuits*. Wiley, 2002. ISBN: 9780471593980. URL: https://books.google.com.tw/books?id=G-dhQgAACAAJ.

[5] E.F. Schubert. *Physical Foundations of Solid-State Devices*. E. Fred Schubert, 2015. ISBN: 9780986382628. URL: https://books.google.com.tw/books?id=l5gSBwAAQBAJ.

[6] U.K. Mishra et al. "GaN-Based RF power devices and amplifiers". In: *Proceedings of the IEEE* 96 (Mar. 2008), pp. 287–305. DOI: 10.1109/JPROC.2007.911060.

[7] E O. Johnson. "Physical limitations on frequency and power parameters of transistors". In: *RCA Rev* 26 (Apr. 1965), pp. 27–34. DOI: 10.1109/IRECON.1965.1147520.

[8] U.K. Mishra, Primit Parikh, and Yifeng Wu. "AlGaN/GaN HEMTs - An overview of device operation and applications". In: *Proceedings of the IEEE* 90 (July 2002), pp. 1022–1031. DOI: 10.1109/JPROC.2002.1021567.

[9] Shuji Nakamura. "GaN growth using GaN Buffer layer". In: *Japanese Journal of Applied Physics* 30 (Oct. 1991), pp. L1705–L1707. DOI: 10.1143/JJAP.30.L1705.

[10] H Amano et al. "Metalorganic vapor phase epitaxial growth of a high quality GaN film using an AlN buffer layer". In: *Applied Physics Letters* 48 (Mar. 1986), pp. 353–355. DOI: 10.1063/1.96549.

[11] Shuji Nakamura, Takashi Mukai, and Masayuki Senoh. "Candela-Class High-Brightness InGaN/AlGaN Double-Heterostructure Blue-Light-Emitting Diodes". In: *Applied Physics Letters* 64 (Apr. 1994), pp. 1687–1689. DOI: 10.1063/1.111832.

[12] Siddha Pimputkar et al. "Prospects for LED lighting". In: *Nature Photonics* 3 (Apr. 2009), pp. 180–182. DOI: 10.1038/nphoton.2009.32.

[13] E.F. Schubert. *Light-Emitting Diodes (3rd Edition)*. E. Fred Schubert, 2018. ISBN: 9780986382666. URL: https://books.google.com.tw/books?id=GEFKDwAAQBAJ.

[14] Dominic King-Smith and David Vanderbilt. "Theory of Polarization of Crystalline Solids". In: *Physical review. B, Condensed matter* 47 (Feb. 1993), pp. 1651–1654. DOI: 10.1103/PhysRevB.47.1651.

[15] L. Vegard. "Die Konstitution der Mischkristalle und die Raumfüllung der Atome". In: *Zeitschrift fur Physik* 5 (Jan. 1921), pp. 17–26. DOI: 10.1007/BF01349680.

[16] Energias Market Research. *Global Gallium Nitride (GaN) Semiconductor Devices Market to Witness a CAGR of 14.2% during 2018-2024*. Oct. 2018. URL: https://www.energiasmarketresearch.com/gallium-nitride-semiconductor-devices-market-size/.

[17] Yole Développement. *Power GaN 2018: Epitaxy, Devices, Applications and Technology Trends*. Dec. 2018. URL: https://www.i-micronews.com/produit/power-gan-2018-epitaxy-devices-applications-and-technology-trends/.

[18] MarketsandMarkets. *GaN Power Device Market - Global Forecast to 2023*. Dec. 2017. URL: https://www.marketsandmarkets.com/Market-Reports/gallium-nitride-wafer-market-93870461.html.

[19] R. Quay. *Gallium Nitride Electronics*. Springer Series in Materials Science. Springer Berlin Heidelberg, 2008. ISBN: 9783540718925. URL: https://books.google.com.tw/books?id=iL%5C_dAR2xyFMC.

[20] Hao Zhang. *Physics Based Virtual Source Compact Model of Gallium-Nitride High Electron Mobility Transistors*. 2017. URL: http://hdl.handle.net/10012/11678.

[21] Sourabh Khandelwal and T.A. Fjeldly. "A physics based compact model of I–V and C–V characteristics in AlGaN/GaN HEMT devices". In: *Solid-State Electronics* 76 (Oct. 2012), pp. 60–66. DOI: 10.1016/j.sse.2012.05.054.

[22] Bing J. Sheu et al. "A compact IGFET charge model". In: *Circuits and Systems, IEEE Transactions on* 31 (Sept. 1984), pp. 745–748. DOI: 10.1109/TCS.1984.1085562.

[23] M.-C Jeng, P.K. Ko, and Chenming hu. "Deep-submicrometer MOSFET model for analog/digital circuit simulations". In: *Technical Digest - International Electron Devices Meeting* (Feb. 1988), pp. 114–117. DOI: 10.1109/IEDM.1988.32766.

[24] W. Liu et al. *BSIM 3v3.2 MOSFET Model Users' Manual*. Tech. rep. UCB/ERL M98/51. EECS Department, University of California, Berkeley, 1998. URL: http://www2.eecs.berkeley.edu/Pubs/TechRpts/1998/3486.html.

[25] Larry Dunleavy et al. "Modeling GaN: Powerful but Challenging". In: *IEEE Microwave Magazine* 11 (2010), pp. 82–96.

[26] I. Angelov, H. Zirath, and N. Rosman. "A new empirical nonlinear model for HEMT and MESFET devices". In: *IEEE Transactions on Microwave Theory and Techniques* 40.12 (Dec. 1992), pp. 2258–2266. DOI: 10.1109/22.179888.

[27] Andrey Kokolov and L I. Babak. "Methodology of built and verification of non-linear EEHEMT model for GaN HEMT transistor". In: *Radioelectronics and Communications Systems* 58 (Oct. 2015), pp. 435–443. DOI: 10.3103/S0735272715100015.

[28] J. Xu et al. "Dynamic FET model - DynaFET - for GaN transistors from NVNA active source injection measurements". In: *2014 IEEE MTT-S International Microwave Symposium (IMS2014)* (June 2014), pp. 1–3. DOI: 10.1109/MWSYM.2014.6848293.

[29] X. Cheng and Y. Wang. "A Surface-Potential-Based Compact Model for AlGaN/GaN MODFETs". In: *IEEE Transactions on Electron Devices* 58.2 (Feb. 2011), pp. 448–454. DOI: 10.1109/TED.2010.2089690.

[30] Ujwal Radhakrishna and Dimitri Antoniadis. "MIT Virtual Source GaN HEMT-High Voltage (MVSG-HV) compact model". In: (Jan. 2015). DOI: 10.4231/D3086365H.

[31] S. Khandelwal et al. "ASM GaN: Industry Standard Model for GaN RF and Power Devices—Part 1: DC, CV, and RF Model". In: *IEEE Transactions on Electron Devices* 66.1 (Jan. 2019), pp. 80–86. DOI: 10.1109/TED.2018.2867874.

[32] S. A. Albahrani et al. "ASM GaN: Industry Standard Model for GaN RF and Power Devices—Part-II: Modeling of Charge Trapping". In: *IEEE Transactions on Electron Devices* 66.1 (Jan. 2019), pp. 87–94. DOI: 10.1109/TED.2018.2868261.

[33] O. Wing. *Gallium Arsenide Digital Circuits*. The Springer International Series in Engineering and Computer Science. Springer US, 2012. ISBN: 9781461315414. URL: https://books.google.com.tw/books?id=i58ACAAAQBAJ.

[34] S. Khandelwal, N. Goyal, and T. A. Fjeldly. "A Physics-Based Analytical Model for 2DEG Charge Density in AlGaN/GaN HEMT Devices". In: *IEEE Transactions on Electron Devices* 58.10 (Oct. 2011), pp. 3622–3625. DOI: 10.1109/TED.2011.2161314.

[35] S. Khandelwal, Y. S. Chauhan, and T. A. Fjeldly. "Analytical Modeling of Surface-Potential and Intrinsic Charges in AlGaN/GaN HEMT Devices". In: *IEEE Transactions on Electron Devices* 59.10 (Oct. 2012), pp. 2856–2860. DOI: 10.1109/TED.2012.2209654.

[36] A.S. Householder. *The Numerical Treatment of a Single Nonlinear Equation*. International series in pure and applied mathematics. McGraw-Hill, 1970. URL: https://books.google.com.tw/books?id=ykOUvgEACAAJ.

[37] X Xi et al. *BSIM4.3.0 MOSFET Model - User's Manual*. Jan. 2003.

[38] S. Khandelwal et al. "Analytical modeling of surface-potential and drain current in AlGaAs/GaAs HEMT devices". In: (Nov. 2012), pp. 183–185. DOI: 10.1109/RFIT.2012.6401654.

[39] S. Khandelwal and T. A. Fjeldly. "A Surface-Potential-Based Compact Model for Study of Non-Linearities in AlGaAs/GaAs HEMTs". In: (Oct. 2012), pp. 1–4. DOI: 10.1109/CSICS.2012.6340055.

[40] F. M. Yigletu et al. “Compact Charge-Based Physical Models for Current and Capacitances in AlGaN/GaN HEMTs”. In: *IEEE Transactions on Electron Devices* 60.11 (Nov. 2013), pp. 3746–3752. ISSN: 0018-9383. DOI: 10.1109/TED.2013.2283525.

[41] Sudip Ghosh et al. “Modeling of Source/Drain Access Resistances and their Temperature Dependence in GaN HEMTs”. In: (Aug. 2016). DOI: 10.1109/EDSSC.2016.7785254.

[42] G.F. Knoll. *Radiation Detection and Measurement*. John Wiley & Sons, 2010. ISBN: 9780470131480. URL: https://books.google.com.tw/books?id=4vTJ7UDel5IC.

[43] A. Ionascut-Nedelcescu et al. “Radiation hardness of gallium nitride”. In: *IEEE Transactions on Nuclear Science* 49.6 (Dec. 2002), pp. 2733–2738. DOI: 10.1109/TNS.2002.805363.

[44] S J. Pearton et al. “Review—Ionizing Radiation Damage Effects on GaN Devices”. In: *ECS Journal of Solid State Science and Technology* 5 (Jan. 2016), Q35–Q60. DOI: 10.1149/2.0251602jss.

[45] Jonathan Lee et al. “Low dose 60 Co gamma-irradiation effects on electronic carrier transport and DC characteristics of AlGaN/GaN high-electron-mobility transistors”. In: *Radiation Effects and Defects in Solids* 172 (Mar. 2017), pp. 1–7. DOI: 10.1080/10420150.2017.1300903.

[46] Alexander Polyakov et al. “Radiation effects in GaN materials and devices”. In: *J. Mater. Chem. C* 1 (Jan. 2013), pp. 877–887. DOI: 10.1039/C2TC00039C.

[47] M G Ganchenkova and Risto Nieminen. “Nitrogen Vacancies as Major Point Defects in Gallium Nitride”. In: *Physical review letters* 96 (June 2006), p. 196402. DOI: 10.1103/PhysRevLett.96.196402.

[48] Ya-Hsi Hwang et al. “Effect of Gamma Irradiation on DC Performance of Circular-Shaped AlGaN/GaN High Electron Mobility Transistors”. In: *ECS Transactions* 61 (Mar. 2014), pp. 205–210. DOI: 10.1149/06104.0205ecst.

[49] J. T. Moran et al. “The Effects of Temperature and Electron Radiation on the Electrical Properties of AlGaN/GaN HFETs”. In: *IEEE Transactions on Nuclear Science* 56.6 (Dec. 2009), pp. 3223–3228. DOI: 10.1109/TNS.2009.2033694.

[50] O Aktas et al. “60Co gamma radiation effects on DC, RF, and pulsed I–V characteristics of AlGaN/GaN HEMTs”. In: *Solid-State Electronics* 48 (Mar. 2004), pp. 471–475. DOI: 10.1016/j.sse.2003.08.003.

[51] G. A. Umana-Membreno et al. “/sup 60/Co gamma irradiation effects on n-GaN Schottky diodes”. In: *IEEE Transactions on Electron Devices* 50.12 (Dec. 2003), pp. 2326–2334. DOI: 10.1109/TED.2003.820122.

[52] A M. Kurakin et al. “Mechanism of mobility increase of the two-dimensional electron gas in AlGaN/GaN heterostructures under small dose gamma irradiation”. In: *Journal of Applied Physics* 103 (Apr. 2008), pp. 083707–083707. DOI: 10.1063/1.2903144.

[53] S.A. Vitusevich et al. “Improvement of interface properties of AlGaN/GaN heterostructures under gamma-radiation”. In: *Applied Surface Science* 255 (Nov. 2008), pp. 784–786. DOI: 10.1016/j.apsusc.2008.07.029.

[54] C. Sharma et al. “Investigation of the Degradations in Power GaN-on-Si MIS-HEMTs subjected to the cumulative γ-ray Irradiation”. In: *2019 European Symposiym on Reliability of Electron Devices* 221 (2019).

[55] A. N. Tallarico et al. “Investigation of the p-GaN Gate Breakdown in Forward-Biased GaN-Based Power HEMTs”. In: *IEEE Electron Device Letters* 38.1 (Jan. 2017), pp. 99–102. DOI: 10.1109/LED.2016.2631640.

[56] Ning Xu et al. “Gate leakage mechanisms in normally off p-GaN/AlGaN/GaN high electron mobility transistors”. In: *Applied Physics Letters* 113.15 (2018), p. 152104. DOI: 10.1063/1.5041343.

[57] Matteo Meneghini et al. “Trapping phenomena and degradation mechanisms in GaN-based power HEMTs”. In: *Materials Science in Semiconductor Processing* 78 (Oct. 2017). DOI: 10.1016/j.mssp.2017.10.009.

[58] Yuhao Zhang et al. “Threshold voltage control by gate oxide thickness in fluorinated GaN metal-oxide-semiconductor high-electron-mobility transistors”. In: *Applied Physics Letters* 103 (July 2013). DOI: 10.1063/1.4815923.

[59] Wataru Saito et al. “Recessed-Gate Structure Approach Toward Normally Off High-Voltage AlGaN/GaN HEMT for Power Electronics Applications”. In: *Electron Devices, IEEE Transactions on* 53 (Mar. 2006), pp. 356–362. DOI: 10.1109/TED.2005.862708.

[60] E. A. Jones, F. F. Wang, and D. Costinett. “Review of Commercial GaN Power Devices and GaN-Based Converter Design Challenges”. In: *IEEE Journal of Emerging and Selected Topics in Power Electronics* 4.3 (Sept. 2016), pp. 707–719. DOI: 10.1109/JESTPE.2016.2582685.

[61] T. Wu et al. “Analysis of the Gate Capacitance–Voltage Characteristics in p-GaN/AlGaN/GaN Heterostructures”. In: *IEEE Electron Device Letters* 38.12 (Dec. 2017), pp. 1696–1699. DOI: 10.1109/LED.2017.2768099.

[62] S. Stoffels et al. “Failure mode for p-GaN gates under forward gate stress with varying Mg concentration”. In: *2017 IEEE International Reliability Physics Symposium (IRPS)*. Apr. 2017. DOI: 10.1109/IRPS.2017.7936310.

[63] A. Stockman et al. “Gate Conduction Mechanisms and Lifetime Modeling of p-Gate AlGaN/GaN High-Electron-Mobility Transistors”. In: *IEEE Transactions on Electron Devices* 65.12 (Dec. 2018), pp. 5365–5372. DOI: 10.1109/TED.2018.2877262.

[64] B. Bakeroot et al. “Analytical Model for the Threshold Voltage of *p* -(Al)GaN High-Electron-Mobility Transistors”. In: *IEEE Transactions on Electron Devices* 65.1 (Jan. 2018), pp. 79–86. DOI: 10.1109/TED.2017.2773269.

[65] Y. Tsividis and C. McAndrew. *Operation and Modeling of the MOS Transistor, Third Edtion International Edition*. OUP USA, 2012. ISBN: 9780199829835. URL: https://books.google.com.tw/books?id=fCOAMAEACAAJ.

[66] M. Si M. A. Alam and P. D. Ye. “A critical review of recent progress on negative capacitance field-effect transistors”. In: *Applied Physics Letters* 114.9 (Feb. 2019). DOI: 10.1063/1.5092684.

[67] M. Kobayashi and T. Hiramoto. "On device design for steep-slope negative-capacitance field-effect-transistor operating at sub-0.2V supply voltage with ferroelectric HfO2 thin film". In: *AIP Advances* 6.2 (Feb. 2016). DOI: 10.1063/1.4942427.

[68] M. Kobayashi et al. "Negative Capacitance for Boosting Tunnel FET performance". In: *IEEE Transactions on Nanotechnology* 16.2 (Mar. 2017), pp. 253–258. DOI: 10.1109/TNANO.2017.2658688.

[69] Asif Khan et al. "Negative Capacitance in a Ferroelectric Capacitor". In: *Nature materials* 14 (Sept. 2014). DOI: 10.1038/nmat4148.

[70] Gustau Catalan, David Jiménez, and Alexei Gruverman. "Ferroelectrics: Negative capacitance detected". In: *Nature materials* 14 (Jan. 2015), pp. 137–9. DOI: 10.1038/nmat4195.

[71] Daniel J. R. Appleby et al. "Experimental Observation of Negative Capacitance in Ferroelectrics at Room Temperature". In: *Nano Letters* 14.7 (2014), pp. 3864–3868. DOI: 10.1021/nl5017255.

[72] Pavlo Zubko et al. "Negative capacitance in multidomain ferroelectric superlattices". In: *Nature* 534 (June 2016). DOI: 10.1038/nature17659.

[73] Sayeef Salahuddin and Supriyo Datta. "Use of Negative Capacitance to Provide Voltage Amplification for Low Power Nanoscale Devices". In: *Nano Letters* 8.2 (2008), pp. 405–410. DOI: 10.1021/nl071804g.

[74] L. D. Landau and I. M. Khalatnikov. "On the anomalous absorption of sound near a second order phase transition point". In: 96 (1954), pp. 469–472.

[75] U. Schroeder, C.S. Hwang, and H. Funakubo. *Ferroelectricity in Doped Hafnium Oxide: Materials, Properties and Devices*. Woodhead Publishing Series in Electronic and Optical Materials. Elsevier Science, 2019. ISBN: 9780081024317. URL: https://books.google.com.tw/books?id=4xuPDwAAQBAJ.

[76] T. Schenk. *Formation of Ferroelectricity in Hafnium Oxide Based Thin Films*. Books on Demand, 2017. ISBN: 9783743127296. URL: https://books.google.com.tw/books?id=AQheDgAAQBAJ.

[77] A. I. Khan et al. "Negative Capacitance Behavior in a Leaky Ferroelectric". In: *IEEE Transactions on Electron Devices* 63.11 (Nov. 2016), pp. 4416–4422. DOI: 10.1109/TED.2016.2612656.

[78] A. Aziz et al. "Physics-Based Circuit-Compatible SPICE Model for Ferroelectric Transistors". In: *IEEE Electron Device Letters* 37.6 (July 2016), pp. 805–808. DOI: 10.1109/LED.2016.2558149.

[79] M.E. Lines and A.M. Glass. *Principles and Applications of Ferroelectrics and Related Materials*. Oxford Classic Texts in the Physical Sciences. OUP Oxford, 2001. ISBN: 9780198507789. URL: https://books.google.com.tw/books?id=p6ruJH8C84kC.

[80] G. Pahwa et al. "Analysis and Compact Modeling of Negative Capacitance Transistor with High ON-Current and Negative Output Differential Resistance—Part I: Model Description". In: *IEEE Transactions on Electron Devices* 63.12 (Dec. 2016), pp. 4981–4985. DOI: 10.1109/TED.2016.2614432.

[81] H. Amrouch et al. “Negative Capacitance Transistor to Address the Fundamental Limitations in Technology Scaling: Processor Performance”. In: *IEEE Access* 6 (2018), pp. 52754–52765. DOI: 10.1109/ACCESS.2018.2870916.

[82] Ujwal Radhakrishna, Sayeef Salahuddin, and D. A. Antoniadis. “Compact model of Negative Capacitance MOSFETs (NCFETs)”. In: 2017.

[83] G. Pahwa et al. “Compact Model for Ferroelectric Negative Capacitance Transistor With MFIS Structure”. In: *IEEE Transactions on Electron Devices* 64.3 (Mar. 2017), pp. 1366–1374. DOI: 10.1109/TED.2017.2654066.

[84] G. Pahwa et al. “Physical Insights on Negative Capacitance Transistors in Nonhysteresis and Hysteresis Regimes: MFMIS Versus MFIS Structures”. In: *IEEE Transactions on Electron Devices* 65.3 (Mar. 2018), pp. 867–873. DOI: 10.1109/TED.2018.2794499.